Earth and Planetary Science Letters, 104 (1991) 513–534
Elsevier Science Publishers B.V., Amsterdam

[CH]

Hydrothermal vent distribution along the East Pacific Rise crest (9°09′–54′N) and its relationship to magmatic and tectonic processes on fast-spreading mid-ocean ridges

Rachel M. Haymon [a], Daniel J. Fornari [b], Margo H. Edwards [b,c], Suzanne Carbotte [a], Dawn Wright [a] and Ken C. Macdonald [a]

[a] *Marine Science Institute and Department of Geological Sciences, University of California at Santa Barbara, Santa Barbara, CA 93106, USA*
[b] *Lamont-Doherty Geological Observatory of Columbia University, Palisades, NY 10964, USA*
[c] *Department of Geological Sciences, Columbia University, Palisades, NY 10964, USA*

Received November 27, 1990; revision accepted March 18, 1991

ABSTRACT

Using the near-bottom ARGO imaging system, we visually and acoustically surveyed the narrow (< 200 m wide) axial zone of the fast-spreading East Pacific Rise (EPR) along 83 km of its length (9°09′–54′N), discovered the Venture Hydrothermal Fields, and systematically mapped the distribution of hundreds of hydrothermal features relative to other fine-scale volcanic and tectonic features of the ridge crest. The survey encompasses most of a 2nd order ridge segment and includes at least ten 4th order (5–15 km) segments defined by bends or small lateral offsets of the ridge crest or axis (Devals). 4th order segmentation of the ridge crest is clearly expressed in the high-resolution ARGO data by the fine-scale behavior of the ridge axis and by changes in the characteristics of the axial zone (axial lava age, extent of fissuring, axial morphology and structure, etc.) across segment boundaries. The distribution and along-strike variability of hydrothermal features corresponds closely to the morphotectonic/structural segmentation of the ridge. On the 2nd order scale, we find that high T hydrothermal activity correlates with: (1) shallowing of the axial magma chamber (AMC) reflector to depths < 1.7 km beneath the ridge axis; and, (2) with the presence of a well-developed axial summit caldera (ASC). Previous work refers to this feature as an axial summit graben (ASG); however, the extent of volcanic collapse along the ASG revealed by the ARGO survey adds to evidence that on fast-spreading ridges it is an elongate volcanic caldera rather than a tectonic graben, and supports the introduction of "axial summit caldera" as a more accurate descriptor. All but 1 of the 45 active high T vent features identified with ARGO are located within 20 m of the margins of the ASC. Despite the significant extent of our track coverage outside the ASC, no important signs of venting were seen beyond the axial zone. On the 4th order scale, the abundance and distribution of hydrothermal features changes across 4th order segment boundaries. We find that high T vents are most abundant where: (1) the ASC is very narrow (40–70 m), (2) the AMC reflector is most shallow (< 1.55 km beneath the axial zone), and (3) the axial lavas are youngest and least fissured. To explain the observed distribution of vent activity, a two-layer model of ridge crest hydrothermal flow is proposed in which 3-D circulation at lower T in the volcanic section is superimposed on top of axis-parallel high T circulation through the sheeted dike complex. In the model, circulation parallel to the ridge axis is segmented at the 4th order scale by variations in thermal structure and crustal permeability which are directly associated with the spacing of recent dike intrusions along strike and with cracking down into the sheeted dikes, especially along the margins of the ASC. Based on ratios between numbers of active high T vents and inactive sulfide deposits along particular 4th order segments, and on corresponding volcanic and tectonic characteristics of these segments, we suggest that the individual 4th order segments are in different phases of a volcanic–hydrothermal–tectonic cycle that begins with fissure eruptions, soon followed by magma drainback/drainage and accompanying gravitational collapse, possible development of an ASC, and onset of hydrothermal activity. The hydrothermal activity may wax and continue for up to several hundred years where an ASC is present. The latest phase in the cycle is extensive tectonic fissuring, widening of the ASC by mass wasting along its margins, and waning of hydrothermal activity. In the ARGO area, where full spreading rates are 11 cm/yr, the entire cycle takes less than ~ 1000 years, and the tectonic phase does not develop where the time interval between eruptions is significantly less than 1000 years.

0012-821X/91/$03.50

1. Introduction

Along the crest of the globe-girdling mid-ocean ridge (MOR) system, magma upwelling from the earth's mantle erupts and freezes into the rigid plates of lithosphere that floor the ocean basins. Magmatic activity and tectonic plate movement and deformation along the MOR are accompanied by voluminous hydrothermal convection of cold seawater through the upper portions of the hot, new plates. This vast hydrothermal circulation facilitates a global-scale transfer of heat and chemicals between the hydrosphere and the lithosphere [1–5], and produces numerous hot springs along the crest of the MOR that are associated with mineral deposits and unique animal communities ([6–8] and references therein). Since the initial discovery of MOR hot springs in the 1970's [9,10], investigations have underscored how much is yet to be learned about seafloor hydrothermal activity and its significant impact on our planet. In this study we address outstanding questions about the interaction and feedback between magmatic, tectonic, and hydrothermal processes on the crest of a fast-spreading MOR.

Hydrothermal flow on the MOR crest is governed by the thermal regime and permeability field in new ocean crust, properties which at present are not well-constrained by direct measurements. Both parameters are strongly coupled to magmatic and tectonic activity along the MOR crest. Until quite recently we knew too little about the spatial and temporal scales of variability in MOR magmatic and tectonic processes to have a realistic context for understanding hydrothermal processes. In the 1980's, however, a compelling new view of MOR processes arose from an impressive confluence of bathymetric, geophysical, and geochemical data (e.g. [11–16]) which indicate that the MOR is supplied with magma from a linear array of discrete mantle magma sources that are discontinuous along the ridge and variable in output. In this new paradigm, the MOR is partitioned along its length into distinct magmatic segments overlying separate melt sources. Because the melt sources do not fall exactly along a line, adjacent ridge segments often are laterally offset, resulting in discontinuities of the ridge axis. An empirical hierarchy of segments has been established based on the nature of the ridge axis discontinuities mapped to date [12,14]. The lengths of segments on the East Pacific Rise (EPR) vary from 300–500 km for 1st order segments (bounded by major transform faults) to approximately 10

Fig. 1. Distribution of tectonic, magmatic, and hydrothermal features of the Venture Hydrothermal Fields along the East Pacific Rise (EPR) crest, 9°09′–9°54′N. Inset map shows location of the survey area on the northern EPR. Sea Beam bathymetry on left was plotted at UCSB using JOI synthesis data [58]. Contour interval for the rise crest is 20 m. Columns on right show distribution of various features along strike, note excellent correlation between 4th order morphotectonic/structural segments and the distribution of hydrothermal features along the ridge. The delineation of the axial summit caldera (ASC) in the leftmost column is based on combined analysis of ARGO sonar data and near bottom imagery (Fig. 4 and Fornari et al., in prep.) and Sea MARC II sonar data (Fig. 4; [29]). The ASC is well-developed (wall-bounded) in the regions denoted by a solid line. The dashed portions of the line denote sections of the ridge axis where the ASC is poorly developed, i.e. where the axial zone exhibits extensive fissuring and/or collapse that is not scarp-bounded on both sides. Almost all high T vents are located near the bounding scarps of the ASC. Using data from Detrick et al. [13], the behavior of the seismic axial magma chamber reflector (AMC REFL.) is shown in the next column to the right. The solid line indicates where an AMC reflector was detected; the dashed line shows where the subseafloor depth of the AMC reflector shoals to 1.7 km or less; and the dotted line marks where the AMC reflector is shallowest (at subseafloor depths of 1.55 km or less). Moving right to the next column, the regions of active high T venting detected by the ARGO survey are represented as solid boxes. Black dots mark the areas where black smoker chimneys or smoke plumes were seen. The dashed boxes are areas where venting of cloudy fluid (lower T?) was observed. Note that high T vents are most abundant where AMC is shallowest. In the column labelled "SULFIDE DEPOSITS", the solid boxes outline areas where mineral deposits were seen with ARGO (both active and inactive). The "VENT BIOTA" column shows the distribution and density of hydrothermal vent fauna along the axial zone, with solid black bars denoting dense vent communities, solid open boxes representing groups of 5–30 animals and dashed boxes denoting 1–5 scattered animals. The arrows in the next column ("HYDROTHERMAL GAPS") denote areas where no evidence for hydrothermal activity is observed in the ARGO data. The rightmost column divides the ridge crest into Deval-bounded, 4th order segments based on subtle bends in Sea Beam bathymetric contours [11,12,17,58] and offsets in the ASC seen in Sea MARC II [29] and ARGO sonar data (Fig. 4). The segment boundaries correlate with distinct along-strike changes observed in axial lava age and flow morphology; presence, structure and morphology of the ASC; extent of axial fissuring, and hydrothermal vent abundance and distribution based on the ARGO data.

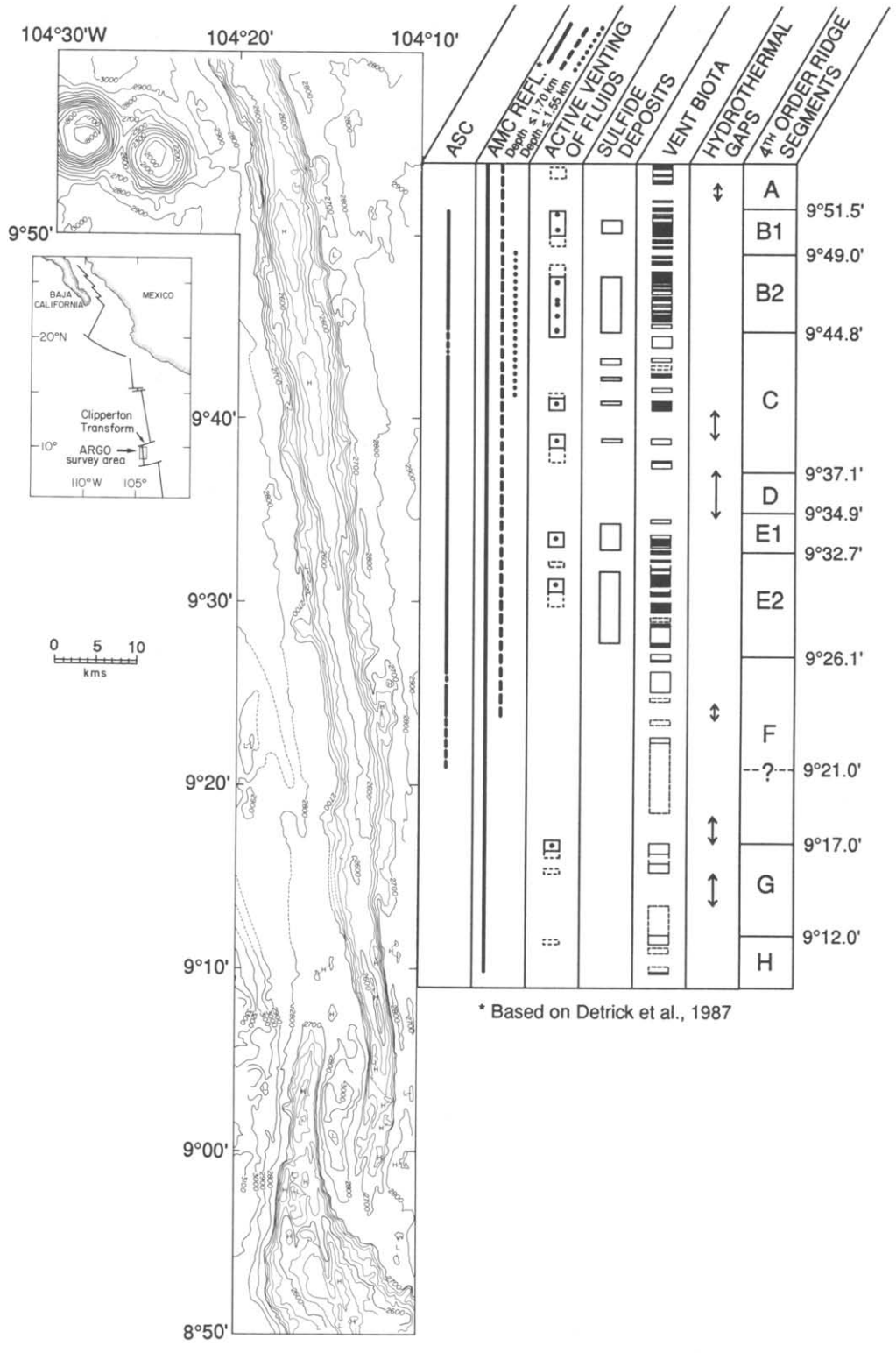
104°30'W
104°20'
104°10'
9°50'
9°40'
9°30'
9°20'
9°10'
9°00'
8°50'
BAJA CALIFORNIA
MEXICO
20°N
10°
Clipperton Transform
ARGO survey area
110°W
105°
0 5 10
kms
ASC
AMC REFL.*
Depth ≤ 1.70 km
Depth ≤ 1.55 km
ACTIVE VENTING OF FLUIDS
SULFIDE DEPOSITS
VENT BIOTA
HYDROTHERMAL GAPS
4TH ORDER RIDGE SEGMENTS
A
B1
B2
C
D
E1
E2
F
G
H
?
9°51.5'
9°49.0'
9°44.8'
9°37.1'
9°34.9'
9°32.7'
9°26.1'
9°21.0'
9°17.0'
9°12.0'
* Based on Detrick et al., 1987

km for 4th order segments (bounded by spreading axis offsets of less than 500 m). The 4th order segments, like the higher order segments, may be associated with independent pulses of mantle-derived melt [12,14,17]. Alternatively, short, small-offset ridge segments may result from misaligned fissure eruptions from longer, more continuous crustal magma reservoirs [11,14] like those seismically detected at depths of < 3 km beneath the EPR crest [13]. 4th order segments could therefore reflect either shallow magma plumbing and delivery processes, or the deeper pattern of mantle magma upwelling, or possibly both.

These new ideas about MOR magma supply processes have profound implications for understanding MOR hydrothermal circulation. However, study of hydrothermal activity at the requisite spatial scale of whole ridge segments requires visual surveys over large areas of seafloor, a technically difficult objective. The global MOR system is ~ 70,000 km in length. Altogether, less than 1% of its length has been visually surveyed thus far, and prior to this study the maximum continuity of systematic vent-mapping along the strike of the ridge was not more than 20 km [5,6,9,18–20,46]. Hence the abundance of vent activity and its distribution relative to other MOR features remains largely unknown.

In this study, we have applied advanced technology for near-bottom imaging of the seafloor to establish the abundance and distribution of hydrothermal vents and deposits for most of a 2nd order ridge segment, including at least ten 4th order segments. Our survey, along a fast-spreading portion of the MOR in the eastern Pacific, provides continuous coverage of an 83 km stretch of ridge crest. This unique data set shows variations in hydrothermal output correlating with specific volcanic, morphological, structural, and geophysical features of the ridge crest (Fig. 1), and reveals along-strike changes in hydrothermal activity related to magmatic processes at the second- and fourth- (5–15 km) order scales of ridge segmentation.

2. Data collection

In November–December 1989, during Leg III of the Venture expedition on R/V *Thomas Washington*, we visually and acoustically imaged the axial zone of the East Pacific Rise (EPR) between 9°09′N and 9°54′N (Fig. 1) in a continuous near-bottom survey along multiple closely spaced tracks (Fig. 2). A deep-towed instrument, the coaxial ARGO imaging system, owned and operated by the Deep Submergence Laboratory of the Woods Hole Oceanographic Institution, was used for this purpose [21]. For our survey, the ARGO was configured with: three video cameras (forward-looking, down-looking, and down-looking zoom) for continuous video imaging; a down-looking electronic still camera for high-resolution, digital imaging [22]; a down-looking 35 mm still camera for color photography; a 100 kHz Klein sonar system for high-resolution side- and forward-looking acoustic imaging; a pressure depth sensor; a 100 kHz narrow-beam acoustic altimeter to determine height above the bottom; a magnetic compass; four 600 watt/s strobes and two 250 watt floodlights; an Ocean Sensors CTD to measure conductivity, temperature, and density of the bottom waters, and a Benthos transmissometer to measure the clarity of bottom waters. The coaxial ARGO system has previously been used for two similar (though less dense and continuous) MOR surveys, including the ARGO RISE survey along parts of the EPR between 10°19′N and 11°53′N [18,23].

The axial zone along most of the surveyed portion of the EPR is less than 200 m wide, and thus a high degree of navigational precision using bottom-moored transponders was required for our survey. By laying out a line of nineteen transponders spaced 1 km west of the ridge axis and ~ 5 km apart, and by using GPS satellite navigation and Sea Beam maps at the outset to fix the positions of these transponders relative to one another, we were able to attain ± 5 m navigational precision within our transponder array for the entire 83 km length of our survey area. This allowed us to drive a series of closely spaced long lines, 10–50 m apart, throughout the area (Fig. 2), and to carry out detailed surveys with line spacings of only 5–20 m over hydrothermal fields. To achieve the optical resolution needed for identification of hydrothermal and geologic features in the video images, we towed ARGO 7–10 m above the bottom. This resulted in a visual swath width of 10–16 m, and an acoustic swath width of ~ 300 m. Given the close spacing of our lines, we

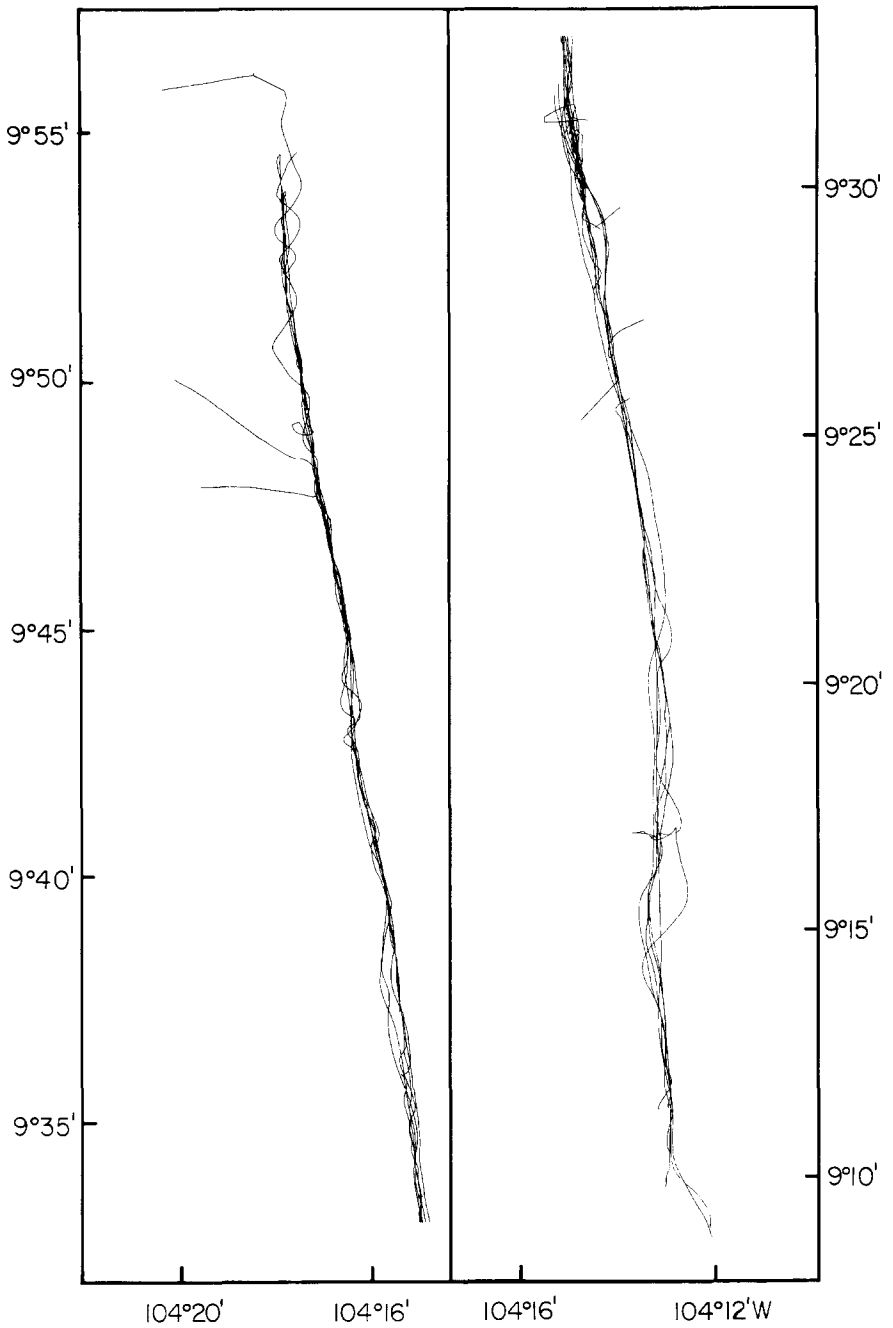

Fig. 2. Tracklines of ARGO survey along the EPR axial zone survey. A total of 28 lines were run. The field area was divided into southern and northern portions at approximately 9°30′N; 13 lines were run in the southern area and 15 lines in the northern area, with extensive overlap in the future ODP drillsite area between 9°29′ and 32′N.

estimate our density of visual coverage at an unprecedented 80% where the ridge axis is well-defined by an axial summit caldera (see section 4.4) and 40% or better along the portions of the ridge where the caldera is poorly developed or absent. The total area imaged visually is roughly 9 million square meters. The density of the sonar coverage is approximately 90%, and the overlapping swaths

cover a 500–800 m wide zone centered on the ridge axis.

3. Description of the tectonic and magmatic characteristics of the EPR crest in the ARGO survey area

The ARGO survey area comprises most of a 2nd order segment along a fast-spreading portion of the EPR (full opening rate = 11 cm/yr; [24]). This segment is bounded to the north, at 10°10′N, by the Clipperton transform fault, and to the south, at 9°03′N, by an overlapping spreading center ("OSC"; a type of ridge axis discontinuity [11,14,25–27]; Fig. 1). The 2nd order segment surveyed includes numerous 4th order segments (discussed below). No 3rd order segments, as defined by Macdonald et al. (1988) [14], occur along this section of the EPR.

In the ARGO survey area, the depth and shape of the EPR vary along strike [11,17,28–30]. Starting at the 9°03′N OSC, the ridge shoals northward from a 2760 m deep, narrow razorback ridge, only 2 km wide and with a triangular cross-section, to a 2540 m deep, 4 km wide ridge with a rectangular cross-section at 9°50′N. A local topographic high is present on the ridge crest at 9°50′N, where the Lamont seamount chain intersects the EPR crest [30]. North of this high, the ridge crest maintains a broad, rectangular shape and is shallower than 2600 m until the western end of the Clipperton transform is reached.

The steady increase in the width and elevation of the ridge crest from the 9°03′N OSC to the intersection of the EPR with the Lamont seamounts has been attributed to a northward increase in mantle magma flux that causes the northern portion of the ridge segment to be magmatically inflated compared to the melt-starved OSC [14,28,30]. This interpretation is consistent with seismic reflection data along the ridge axis in this area [13]. The seismic reflection studies reveal the presence of a nearly continuous seismic reflector, thought to be the top of an axial magma chamber (AMC), at depths of 1.5–2.5 km beneath the seafloor. The only gap in this reflector coincides with the location of the 9°03′N OSC (Figs. 1 and 3). Altogether, the high elevation of this section of the EPR compared to adjacent ridge segments [28], the signal strength of the seismic reflector [13], the relatively homogeneous compositions of lavas erupted north of the OSC in this area [12,31], and the burial of ridge crest faults and fissures by recent volcanism (observed in Sea MARC I sonar records and near-bottom photos taken between 10°5′ and 10′N; [32]) mutually suggest unusually enhanced magmatic activity on this segment of the EPR.

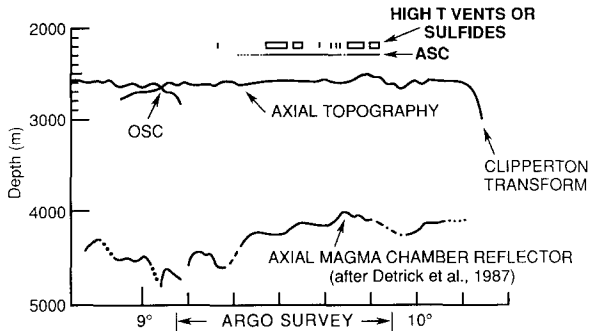

Fig. 3. Correlation plot modified from Macdonald and Fox [28] showing: (1) EPR axial depth profile, from Sea Beam data [11,28]; (2) depth to the AMC reflector, based on seismic reflection data [13,33]; (3) locations of areas along the axial zone (solid boxes and vertical bars) where high T hydrothermal vents and/or sulfide deposits occur, based on the ARGO visual data; and, (4) location of the ASC, based on ARGO sonar records (Fig. 4; Fornari et al., in prep.) and Sea MARC II sonar data (Fig. 4; [29]). Solid line denotes well-developed ASC, dashed line represents poorly developed ASC. Note that high T vent activity and sulfide deposition occur where the AMC is shallow and the ASC is well-developed. AMC reflector is dotted where the multichannel seismic profile along the ridge crest may be slightly off-axis [28], and is dashed where the reflector is present but weak as interpreted by Detrick et al. [13].

The location of the ridge axis in this area as determined from Sea MARC II side-looking sonar records [29] is shown in Fig. 4. From north to south, the axis steps west in a series of right-stepping, en echelon, 4th order segments < 15 km in length. South of 9°28′N, seismic data show that the position of the magma chamber axis lies ~ 3 km to the west of the topographic ridge axis [17,33]. Possibly the topographic ridge is stepping west to recenter itself over the present axis of the magma chamber.

From the character of the axial trace in Sea MARC II side-looking sonar records, an "axial summit graben", i.e. a linear trough bounded by opposing scarps, has been identified along much of the EPR axis in the ARGO survey area [29].

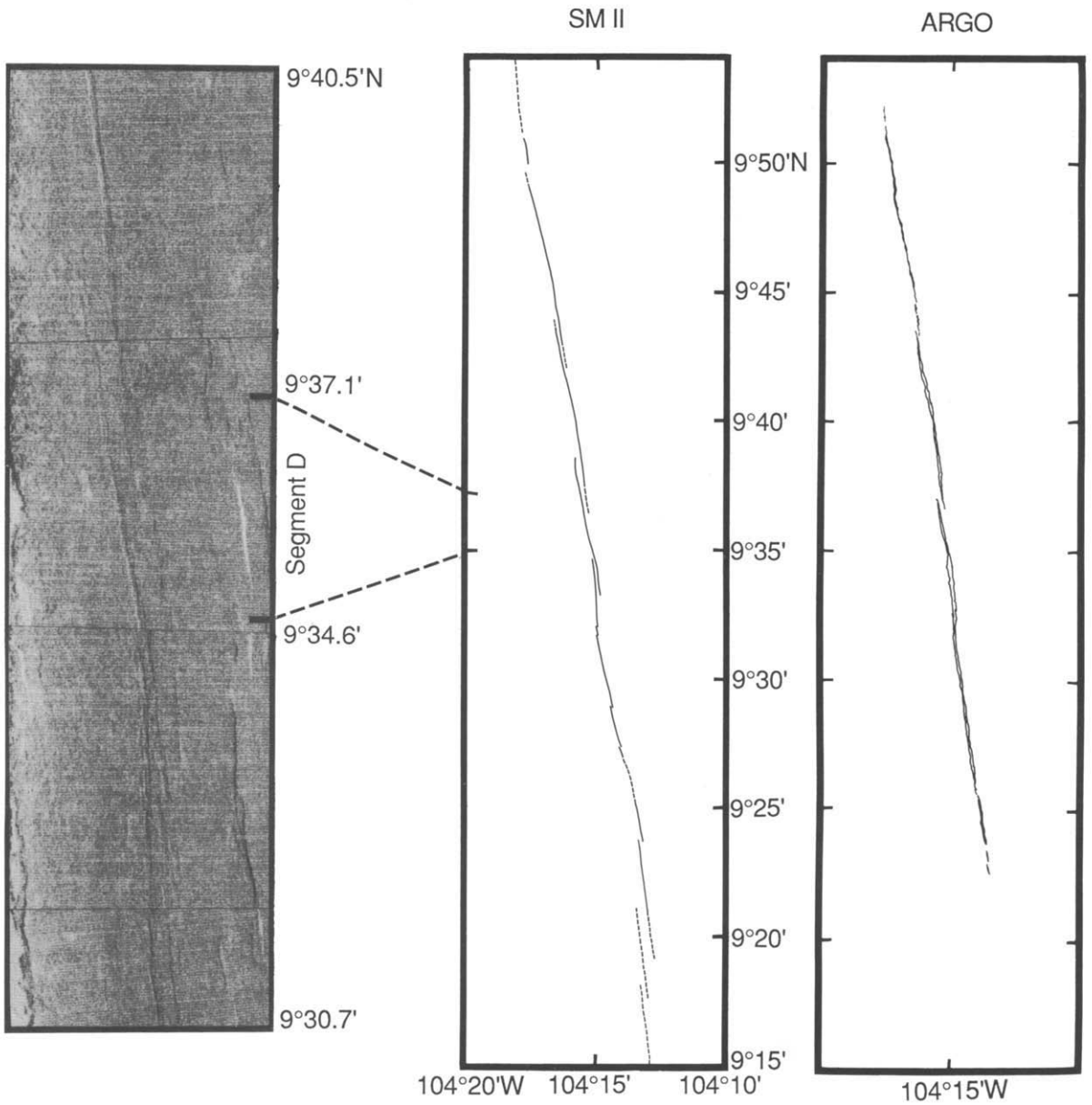

Fig. 4. EPR plate boundary configuration in the ARGO survey area. On left, blow-up of Sea MARC II sonar record between approximately 9°30′ and 42′N showing paired black acoustic reflectors and white shadows characteristic of a well-developed ASC. In middle, plate boundary determined from Sea MARC II (SM II) sonar data, 9°54′–15′N, from Macdonald et al. [29]. The presence of the ASC is denoted by a solid line; the dashed line shows where the axial zone appears as a discontinuous, "fuzzy" trace in the Sea MARC II records. On right, ASC configuration determined from ARGO sonar records. Width of the ASC is measured across the top of this feature between the outermost bounding walls. Agreement between Sea MARC II and ARGO delineation of the ASC is excellent considering the difference in resolution and areal coverage for the two systems.

For reasons discussed below (section 4.4) we have chosen to rename this feature "axial summit caldera" and refer to it throughout as the "ASC". The presence of the ASC in the Sea MARC II data is indicated in Fig. 4 by a solid line. Where the plate boundary is dashed in Fig. 4, there is no distinct ASC in the records, although the axial zone can still be distinguished as a fuzzy narrow

band of higher reflectivity and closely spaced fissures. The ASC does not show up on Sea Beam maps contoured at 10 m depth intervals, which suggests that it is rarely > 15 m deep [11,17,58]. Macdonald and Fox [28] note a strong spatial correlation between the occurrence of an ASC along the EPR between 9 and 13°N, and: (1) the presence of a strong AMC reflector; (2) shallow axial depths; and (3) a broad cross-sectional shape to the ridge crest. They propose that these features develop where the magma budget of the ridge is high.

Based on a combined analysis of ARGO sonar records (this study, Fig. 4; Fornari et al., in prep.), Sea MARC II sonar data ([29], Fig. 4), and Sea Beam bathymetry ([11,17,29,30,34]; Fig. 1), we have divided the ARGO survey area into morphotectonically/structurally defined 4th order ridge segments labelled A–H (Fig. 1). The segment boundaries are placed at "Devals" (deviations from axial linearity [12]) arising from either offsets in the ridge axis, changes in the trend of the ridge axis and the ridge crest bathymetric contours, or (usually) both (see Table 2). We did not put in boundaries where the lateral distance of ridge axis offset is less than 50 m. Where offsets in the axis occur as a series of en echelon steps, we arbitrarily chose the boundary at the northern onset of stepping. Our boundaries all lie within 3.8 km of 4th order boundaries picked by Macdonald et al. [29] on the basis of Sea Beam and Sea MARC II data. We consider the two studies to be in excellent agreement, given the much finer resolution of the ARGO data compared to Sea MARC II or Sea Beam data, the more restricted areal coverage of the ARGO data, and the subjectivity involved in picking boundaries in areas where the ends of segments overlap (Fig. 4) or exhibit multiple steps.

The ridge-axis offsets at 9°17′N and 9°51.5′ were identified previously by Langmuir et al. [12], although these authors placed the 9°51.5′N boundary at around 9°53′N. In general, basalts recovered from within the ARGO survey area exhibit homogeneous, depleted normal MORB compositions; however, there are subtle changes in the Fe and Si composition of eruptives on either side of the 9°17′N Deval (C. Langmuir, pers. commun.) and distinct magma fractionation sequences on either side of the 9°53′N Deval [12]. Such compositional variations may reflect separate magma sources, differences in partial melting, differences in plumbing, or poor magma mixing across these offsets [11–14,31]. Seismic tomography data beneath the EPR crest show a narrowing of the seismic low-velocity volume at 3 km depth beneath the ridge at 9°28′N and 9°35′N,

TABLE 1

Age scale used in analysis of ARGO bottom photographs

SCALE	DESCRIPTION	VERY APPROXIMATE AGE SCALE FOR 9°N AREA
1.0	No sediment cover, highly vitreous luster	<50 years old
1.2	Light "peach fuzz" of sediment cover, vitreous luster	<100 years old
1.5	Light sediment cover within grooves and cracks in pillows, vitreous luster diminished, no sediment pockets	<500 years old
1.7	No vitreous luster, very small sediment pockets (~2 cm across) on and between pillows	<1000 years old
2.0	Sediment pockets well developed between pillows	1000-5000 years old
3.0	Sediment pockets deep enough to connect between pillows	5000-20,000 years old

*Modified slightly from scale for the EPR crest at 20°S published in Macdonald et al. (1988) [26], based in part on previous work by Ballard et al. (1981) [35]. Regional sedimentation rates in the two areas are similar [2 cm/1000 years near 20°S (McMurtry et al., 1981) [59], compared to 2.3 cm/1000 years near 9°N (Lonsdale and Spiess, 1980) [36].]

TABLE 2

Capsulated descriptions of the principal volcanic, tectonic, and hydrothermal characteristics of the 4th order segments of the EPR from 9°09′ to 54′N based on the ARGO data, SeaMARC II, Sea Beam and seismic data as referenced in text

SEGMENT	CRITERIA FOR SELECTING SEGMENT BOUNDARIES+	VOLCANIC, TECTONIC, AND HYDROTHERMAL CHARACTERISTICS OF SEGMENTS	VERY APPROXIMATE AVERAGE AGE OF AXIAL LAVAS*
A 9°54′-51°5′N	9°54′N: Northern boundary of ARGO survey area. 9°51.5′N: Ridge crest bends and changes trend; ASC appears in ARGO records.	Lobate pillow lavas cut by fissures and lava channels. No ASC north of 9°51.5′N. Low T vents.	Age 1.5 100-500 years
B1 9°51.5′-49.0′N B2 9°49.5′-44.8′N	9°49.0′N: Bathymetry of ridge crest shows subtle offset; ridge axis bends and changes trend slightly; ASC is offset ~50m to the right in ARGO sonar records. 9°44.8′N: Bathymetry of ridge crest shows small offset; ASC tapers and loses definition in ARGO sonar records, axial zone continues as en echelon fissure swarm; SeaMARC II records show small right step of ASC.	Narrow ASC (40-70m) containing many high T vents. "Smoking slot." ASC floor exhibits fresh sheet flows, auto-brecciated lavas, lava pillars, lobate collapse remnants/rubble, and few fissures. ASC steps ~40m left at 9°47.1′N. At 9°45.2′N, ASC tapers, and at 9°44.8′N it degrades into a zone of right-stepping fissures.	Age 1.0 < 50 years
C 9°44.8′-37.1′N	9°37.1′N: Bend in bathymetry of ridge crest and in the ridge axis; ASC steps 400m right in ARGO sonar records.	Large fissures (5-20m wide) continue down to 9°43.5′N, where a wider (150-210m), deeper (15m) ASC takes form and continues southward to end of segment. High T vents present along ASC margins, but less frequent than in Segment B, while fissures in ASC are more frequent.	Age 1.2 50-100 years
D 9°37.1′-34.9′N	9°34.9′N: Bend in bathymetry of ridge crest and in the ridge axis; ASC steps right on SeaMARC II records and appears to bend in ARGO sonar records.	ASC continues southward, 100-150m wide. Contains linear troughs (10-20m wide). No hydrothermal vents and very sparse vent biota.	Age 1.5 100-500 years
E1 9°34.9′-32.7′N E2 9°32.7′-26.1′N	9°32.7′N: Small bend in ASC. Ridge axis steps right ~60m in ARGO records. 9°26.1′N: ASC tapers and loses definition at 9°26.1′N in ARGO sonar records.	Segment E1 has widest ASC in survey area (150-400m). Along E2, ASC is 90-150m wide, 8-15m deep. Extensive collapse within ASC from magma drainback or drainage. Increase in fissure frequency relative to segments B-D. Sparse high T vents and numerous inactive mineral deposits along ASC margins.	Age 1.7 500-1000 years
F 9°26.1′-17′N	9°17′N: Bend in ridge crest bathymetry and sharp kink in ridge axis. Axial trace on SeaMARC II records steps a total of 1.1 km right between 9°19′N and 9°17′N.	ASC degrades into a zone of linear collapse troughs and fissures south of 9°26.1′N, and is scarp-bounded on both sides only from 9°25.5′N to 9°23.7′N. Axial zone is highly fissured south to 9°21′N, where the degraded ASC is buried beneath extremely fresh, unfissured lobate lavas that continue to the end of the segment. No active hydrothermal vents or any mineral deposits found. Very sparse vent biota.	9°26.1′-21′N: Age 2.0 1000-5000 years 9°21′-17′N: Age 1.0 <50 years
G 9°17′-12′N	9°12′N: Bend in ridge crest bathymetry; ridge axis bends and changes trend.	No ASC. Axial zone dominated by fresh, unfissured lobate and pillowed lava flows to 9°14′N. Isolated outcrops of fresh lavas on top of older flows continue to 9°12′N. One high T vent at 9°16.8′N, no mineral deposits.	9°17′-14′N: Age 1.0 <50 years 9°14′-12′N: Age 1.0-1.5 50-500 years
H 9°12′-09′N	9°09′N: Southern boundary of ARGO survey area.	Narrow, steep-sloped pillow ridge. Occasional low T vents and vent biota.	Age 1.5 100-500 years

+ Refer to Figures 1 and 4

*Refer to Table 1

possibly indicating a pinching of the axial magma chamber near both ends of segment E in Fig. 1 [17].

4. Results of the ARGO survey

Within our survey area, we observe significant variability along-strike in apparent lava age (qualitatively estimated according to criteria established by previous near-bottom investigations of fast-spreading ridges [18,26,36]; see Tables 1 and 2); in the morphology of the lavas and structure of the axial zone; and in the degree of tectonization of the axial zone. We find that this variability is expressed on two spatial scales: the 2nd order scale (encompassing the entire 83 km long survey area); and the 4th order scale (5–15 km).

4.1. Second-order features

When the survey area as a whole is considered, the following observations emerge:

(1) The axial zone along this portion of the ridge is dominated by young volcanism (Table 2), which confirms previous speculation about the magmatic robustness of the EPR in this area. The youngest axial lavas (0–50 years old) are found along the shallowest part of the ridge axis, between 9°37′N and 9°51.5′N, and on either side of the 9°17′N Deval (from 9°12′N to 9°21′N).

(2) A well-developed ASC with bounding walls on both sides is confirmed along ~ 80% of the ridge axis between 9°24′N and 9°54′N. This feature occurs along a portion of the ridge where axial depths are above 2600 m and where the AMC reflector shallows to depths less than 1.7 km beneath the seafloor (Figs. 1 and 3). The average width of the ASC is narrowest (40–70 m) above the shallowest part of the AMC reflector and is wider (90–150 m) south of ~ 9°44′N, where the AMC reflector deepens by 100–200 m. South of 9°24′N, the bounding walls of the ASC become subdued, and the poorly defined caldera disappears as a distinct feature at about 9°21′N, where the depth to the AMC reflector sharply increases.

(3) Density of fissuring in the axial zone is higher south of 9°34′N, except in the area of fresh flows between 9°12′N and 9°21′N, and average widths of fissures are correspondingly smaller south of 9°34′N (Wright and Haymon, in prep.). ARGO data show that, in general, lava age and fissure density are correlated (Wright and Haymon, in prep.; Table 2).

In summary, ARGO data show that the seafloor at the ridge axis on average gets older and more fissured as the ridge axis deepens away from the axial high at 9°50′N toward the boundaries of the ARGO survey area, except for the area of young volcanism at 9°21′–12′N. A previous near-bottom Deep-Tow photo/acoustic survey of the OSC at 9°03′N documented similar increases in lava age and fissuring along the ridge axis south of 9°09′N to the southern tip of the ridge segment at 9°00′N [27]. With the ARGO data we further establish that the southward increases in axial depth, axial lava age, and fissuring are accompanied by a widening of the ASC south of ~ 9°44′N, and a degradation of the ASC south of 9°27.5′N until it disappears at about 9°21′N. These changes are spatially correlated with increases in the depth of the magma chamber beneath the ridge axis, and may result from possible decreases in the volume of magma or partial melt residing beneath the ridge axis approaching the OSC, as previous investigators have proposed [27,28].

4.2. Fourth-order features

We find that the fine-scale volcanotectonic features of the axial zone (e.g., lava age, small-scale seafloor morphology and structure, ASC development, fissuring, etc.) change character every 5–15 km along the strike of the ridge, and that these changes usually occur at or near the morphotectonically/structurally defined boundaries of 4th order segments (A–H; Fig. 1). We thus confirm that Deval-bounded, 4th order segmentation of the EPR is expressed in the fine-scale features of the axial zone. A brief description of the individual 4th order segments and the criteria for choosing their boundaries are summarized in Table 2.

There is some uncertainty in choosing the boundaries of Segment F (9°26.1–9°17′N). It is possible that this segment should be subdivided into shorter segments. At 9°21′N the ASC disappears and contacts are observed in ARGO images between the oldest and youngest axial lavas in the ARGO survey area. We have tentatively dashed in a segment boundary at this latitude in Fig. 1.

However, from the ARGO data we could not establish the location(s) of the eruptive center(s) for the fresh lavas we observed. It is possible that the morphology and structure of the ridge crest between 9°21′ and 9°17′N has been modified by extensive outpourings of lava from the axial high centered at about 9°15′N (Fig. 1). Alternatively, magma may have flowed downhill from the north through subsurface lava tubes which intersect the seafloor at ~9°21′ N. Given these uncertainties we have placed the boundary between Segments F and G at 9°17′N where a distinct Deval occurs [12]. We predict that the changes in lava compositions observed across this Deval (C. Langmuir and J. Bender, pers. commun.) are compositional differences between the older lavas found north of 9°17′N and the fresh young lavas which have flowed over them. Note that we have picked the northern boundary of Segment F at 9°26.1′N, where a break in the continuity of the ASC occurs. Toomey et al. [17] and Macdonald et al. [29] placed this boundary 3.5 km further north at 9°28′N where the bathymetric contours of the rise crest in their Sea Beam maps appear to bend. The fact that no sinuosity or discontinuity of the ASC is present in the ARGO sonar records at 9°28′N where the ridge crest contours bend could mean that segment E2 has recently lengthened southward from 9°28′N to 9°26.1′N.

The average width of the ASC south of 9°44′N is 90–150 m, however the ASC briefly widens to 400m along segment E1. This appears to be the result of overlap between segment D and segment E1 which essentially doubles the ASC width in the overlap region.

4.3. The development and evolution of 4th order segments

We can explain the segment-to-segment variations described in Table 2 by ascribing the development of 4th order segmentation to spatial shifts in the locus of individual volcanic dike swarms and eruptions along the ridge over time. The true cause(s) of these shifts, i.e. the principle cause(s) of 4th order segmentation, cannot be firmly established on the basis of present data. The systematic right-lateral stepping of segments along the ridge (Fig. 4) may indicate that the ridge axis is adapting to changes in the location of the axial magma chamber [33,54] as well as to changes in the direction of spreading [29]. Along-strike pinching and swelling of the seismic low-velocity zone beneath the ridge led Toomey et al. [17] to agree with previous speculation [12,14] that 4th order ridge segmentation arises from a segmentation of the magma chamber itself at the 5–15 km scale, due to the distribution of magma sources in the mantle beneath the ridge crest. There are two important debatable issues here. (1) Whether pinching and swelling of the axial magma chamber along strike is due to deep magma supply or to some other mechanism (such as crustal or subcrustal magmatic plumbing; convection in the axial magma chamber; deep hydrothermal cooling; etc.). And (2) whether 4th order segmentation of the magma chamber is the sole or most common cause of the shifts in the locus of magmatic intrusion and eruption which, in turn, are responsible for 4th order segmentation of the ridge crest. Clearly the ultimate origin(s) of 4th order segmentation is not resolved and requires further investigation.

The correlation seen in the ARGO data between axial lava age and fissuring density (Table 2; Wright and Haymon, in prep.) suggests that each 5–15 km segment is in its own phase of a volcanic–tectonic cycle that begins with fissure eruptions, continues with a phase of magma drainback or runoff and consequent gravitational collapse, and concludes with tectonic cracking. Volcanic/tectonic cycles have been postulated by previous investigators [14,35,37–40], but have not been well-constrained in space and time. At a spreading rate of 11 cm/yr, a strip of seafloor the width of the axial zone in the ARGO survey area (40–150 m) is generated in a time period on the order of 10^2–10^3 years, a time interval that agrees rather well with the young ages of lavas observed inside the ASC (Table 2). This agreement suggests that eruption frequency is usually high enough to keep pace with spreading throughout most of the survey area. North of Segment D, where lavas are typically < 100 years old and exhibit a low density of fissuring, eruption frequency may be so often that it precludes the tectonic phase of the cycle. Maximum axial lava ages (1000–5000 years) are observed along the northern portion of Segment F between 9°26′N and 9°20′N, where ongoing spreading in the absence of eruptions has resulted in extensive fissuring. The appearance of

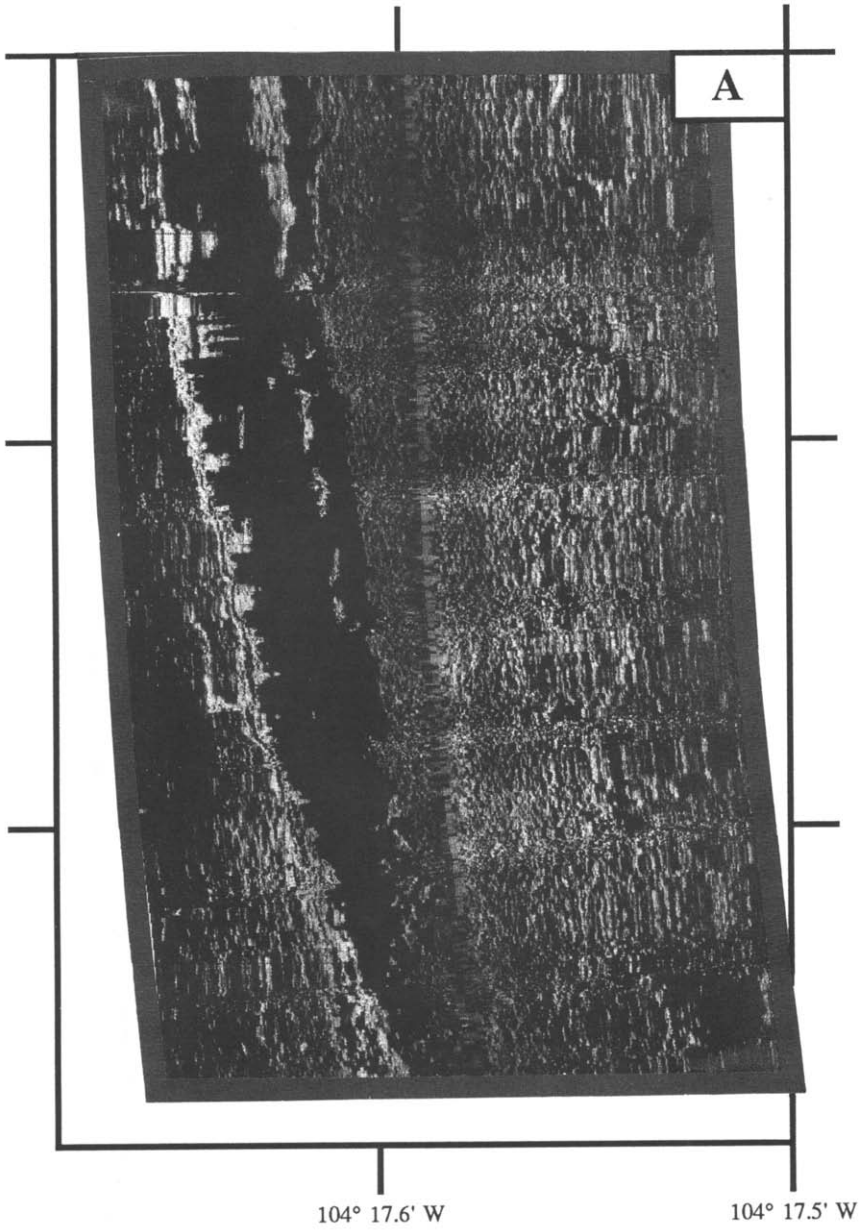

Fig. 5. A. ARGO 100 kHz sonar image recorded on Line 19. White areas are strong acoustic reflectors and black is acoustic shadow (opposite of Sea MARC II record in Fig. 4). Total width of record is ~ 300 m. B. Interpretative sketch of sonar image shown in A with the ASC outlined. Heavy line denotes limit of the sonar image. The eastern ASC wall is well-defined by the start of the acoustic shadow. An area along the western wall has been traced to show the prominent shadows cast by the eastern wall on the highly reflective terrain of the western wall. Within the ASC floor, especially along its eastern margin, a linear array of reflectors (shown by stippled areas) is interpreted either as uncollapsed remnants of the volcanic roof which once existed over the area now occupied by the ASC or as a linear volcanic construct formed by fissure eruptions. The jagged shadows cast by the eastern ASC wall are formed by overhanging, large uncollapsed volcanic crusts that were often visually observed when ARGO was towed along the upper rim of the ASC. The scalloped (in plan-view) character of the ASC walls, the uncollapsed roof remnants, and the often-observed volcanic pillars, collapse pits, and collapse debris within the floor of the ASC all suggest that the ASC is largely a collapse feature associated with magma drainback or drainout.

significant collapse and fissuring along Segment E (where axial lavas are 500–1000 years old) indicates that a complete volcanic–tectonic cycle has transpired within this time interval.

4.4. *Morphology of the axial summit caldera*

From ARGO side-looking sonar data we have precisely mapped the ASC (Fig. 4) and determined that its morphologic and structural character are highly variable along the ridge crest. Detailed discussion and interpretation of the ARGO sonar data, and an explanation of the data processing methods used, are presented elsewhere (Fornari et al., in prep.). The width of the ASC shown in Fig. 4 is the distance between the outermost bounding walls, i.e. the width across the top of the ASC. Where the bounding walls are stepped, the width across the ASC floor is much narrower than the width across the top.

The very fine-scale resolution (1–10 m) of the ARGO sonar data has made it possible for us to see the extreme along-strike variability displayed by the walls and floor of the ASC. Because this variability occurs at very short wavelengths (tens to hundreds of meters), we have defined the ASC

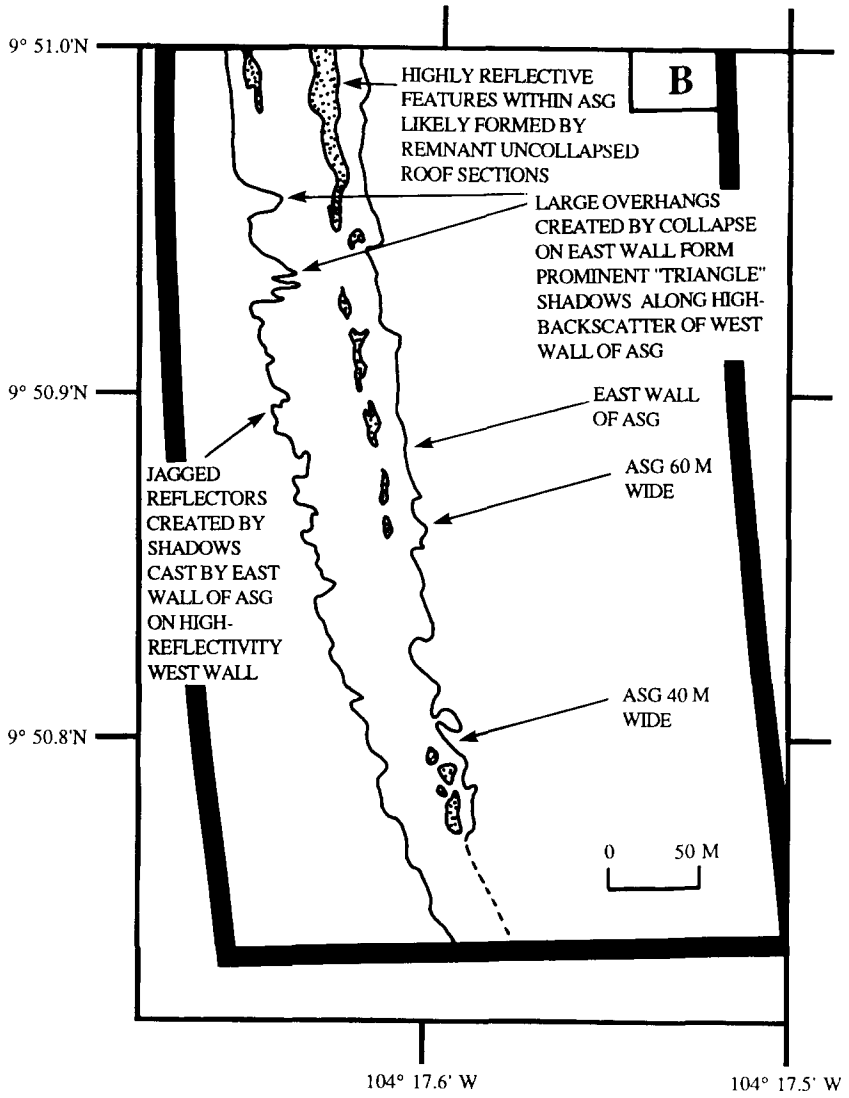

Fig. 5 (continued).

as "present" (solid line in Fig. 1) where it forms a strike-continuous trough that is > 1 km long and > 40 m in width, with well-defined acoustic reflectors from opposing walls > 5 m in height.

Most of the along-strike variability exhibited by the ASC is due to magmatic processes at the 4th order scale. For example, one wall of the ASC may terminate abruptly where it is buried by a recent lava flow (as on the northern portion of Segment F). An important result of the sonar data analysis is the finding that the walls of the ASC are commonly jagged or scalloped in plan-view (Fig. 5). Video images verify that a jagged, sometimes overhanging, lip forms at the margins of the ASC from ragged collapse remnants. Along much of the ASC in the ARGO survey, visual images reveal evidence for extensive collapse, including abundant lava pillars supporting roof remnants, ubiquitous collapse pits, and widespread collapse rubble. Thus in many places the ASC is a syn- or post-volcanic collapse feature, not a purely extensional tectonic graben. This is particularly true where the ASC is narrow (40–70 m wide), as in Segment B (Fig. 5). Where the ASC is wider (150 m), it may have a shallow (< 5 m deep) inner trough nested within a wider outer trough. The walls bounding the inner trough are jagged from collapse, while the walls bounding the outer trough are straightened from fissuring and mass wasting of large blocks, much as described in the 200–250 m wide ASC on the EPR near 13°N by Gente et al. [38].

The ARGO data strongly support the hypothesis that on fast spreading centers the feature referred to in previous work as an "axial summit graben" is actually an elongate axial summit caldera, resulting from the gravitational collapse which follows magma withdrawal in an extensional stress regime. This idea was first proposed by Lonsdale [41] based on Deep-Tow studies of the EPR crest at 3°25′S, and was strengthened by the spatial correlation between the presence of an ASC and the occurrence of an AMC reflector documented by Macdonald and Fox [28]. Given the confirming evidence provided by our fine-scale visual and sonar ARGO observations, we propose that the terminology of "axial summit graben" (ASG) be abandoned in the future in favor of "axial summit caldera" (ASC). We suggest that the character of the floor and walls of this feature, and its dynamic behavior in time, are all best understood by analogy with volcanic calderas. The bounding scarps are quite similar to ring-faults (albeit in a line-source extensional environment rather than a point source setting), and are subject to outward migration and extensive mass-wasting when the depth to the magma chamber increases [38,42]. The depth of the floor varies along-strike and over time in probable concert with changes in the magma pressure from below [28].

5. Abundance and distribution of hydrothermal vents in the Venture Hydrothermal Fields

5.1. Description and classification of hydrothermal features

Prior to the ARGO survey, very little was known about hydrothermal activity along the EPR from 9 to 10°N; however, the occurrence of hot springs here was considered likely in view of morphological and geophysical evidence for a high magma budget, measurements of anomalously warm bottom water temperatures [43] along this part of the EPR, and submersible observations on the axis at 9°53′N of hydrothermally stained lavas and vent fauna [30]. Expectations were confirmed by the ARGO survey, which located hundreds of geologic and biologic hydrothermal features along the axial zone. These hydrothermal phenomena are now designated as the Venture Hydrothermal Fields. The wide range of hydrothermal phenomena seen with ARGO are broken down into active and inactive categories, and into high-temperature (high T) and lower-temperature (low T) categories (Fig. 1 and Table 3).

For the purposes of this study, we define "active vents" as sites where active discharge of fluids or live vent animal communities are seen in the ARGO video and still images. We classify active vents as high or low T based on the visual characteristics established for high and low T vents by previous submersible studies of MOR hot springs [6,9,19,20,44–48]. Active high T vents (> 200°C) are those where visible fluid discharge is accompanied by precipitation of mineral particulates and deposits. This includes all "smoker" vents, i.e. vents where fluids colored by suspended mineral particulates issue from mineralized constructions (Fig. 6A). Varieties recognized in the ARGO

survey include black and white smokers (as defined by Spiess et al. [9]), and "grey" smokers exhibiting flow rates and densities of plume particulates intermediate between those of black and white smokers. From previous studies of EPR vents [4,9,49–52], we presume that the temperatures of black smoker fluids are 350–400°C, and that the temperatures of white smoker fluids are 200–330°C. A submersible dive program in the ARGO survey area scheduled for 1991 will determine discharge temperatures for the different vent types in this area and provide greater detail about the properties of vent fluids and mineral deposits.

Active low T vents appear in ARGO images as milky, cloudy, or shimmering effluents venting from cracks and crevices in the basaltic seafloor. There are no mineral deposits forming on the seafloor at these vents, although some encrustations or staining of basalt are often seen. At very low flow rates, no fluid can be detected by the ARGO cameras, but dense colonies of vent organisms are present, including vestimentiferan tube worms, polychaete tube worms, serpulid worms, vesicomyid clams, mussels, brachyuran and galatheiid crabs, and various fish.

Inactive vents are sites where mineral deposits and encrustations, hydrothermal sediments, or hydrothermal staining of basalts are found in the absence of fluid discharge and live vent fauna. Inactive high T sites in the ARGO survey area include sulfide constructions classified as follows: chimneys = cylindrical or conical constructions up to several meters in height; edifices = larger, more complex constructions up to 20 m in height and several meters in diameter, often topped by several chimneys (Fig. 6A and B); mounds = elongate, low-relief massive sulfide accumulations meters to several tens of meters long; and, encrustations = sulfide layers up to several centimeters thick precipitated on a basalt substrate. Inactive low T sites are areas where the only hydrothermal indicators are minor staining of basalts, patchy hydrothermal sediment, and/or dead vent organisms.

5.2. *Abundance and distribution of vents: 2nd order features*

The portions of the axial zone where active high T vents (i.e., smokers) occur are shown by the solid boxes in Fig. 1 (see third column from left). The dashed boxes indicate active areas of low T venting. Black dots mark the locations of the hottest vents, where either black smokers or black smoke plumes appear in ARGO images. In the adjacent column to the right, areas of sulfide deposition (active and inactive) are indicated by solid boxes. The distribution and density of hydrothermal vent animals are given in the column labelled "Vent Biota". In the column labelled "Hydrothermal Gaps", arrows delineate portions

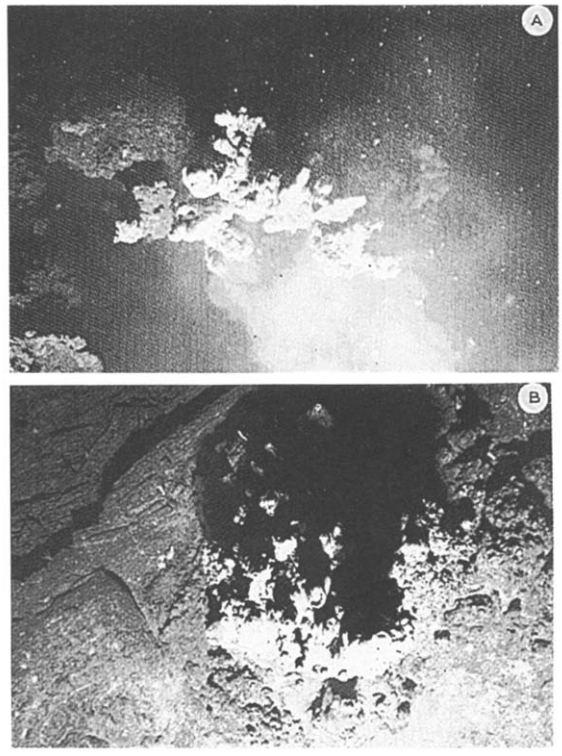

Fig. 6. A. Top view of an active black smoker edifice along the base of the west wall of the ASC in Segment B2 near 9°45′N. Electronic Still Camera (ESC) image, depth 2540 m, altitude = 7.0 m, heading 350° (towards top of image). Horizontal width of image is ~ 4 m. Note "smoke" plume which is wafting from the chimney spires. Edifice is ~ 7 m high and ~ 2 m wide near the top; note that several smaller chimneys have coalesced to form the top of the edifice. B. Top view of inactive sulfide edifice near the east wall of the ASC in Segment C near 9°41′N. Electronic Still Camera (ESC) image, depth 2560 m, altitude = 8.0 m, heading 350°(towards top of image). Horizontal width of image is ~ 4.8 m, image area = 15.6 m^2. Edifice is ~ 6 m high and ~ 2.2 m wide near the top; note numerous small chimneys which extend upward from the top of edifice. The edifice appears to be a complex structure created by coalescence of the smaller chimneys.

TABLE 3A

Locations of vents actively discharging high-temperature [a] hydrothermal fluid

Black smoker	
Segment B1:	[9°50′17.7″, 104°17′29.1″; 9°50′17.7″, 104°17′28.7″; 9°50′16.8″, 104°17′29.5″]
Segment B2:	9°46′16.6″, 104°16′44.4″; 9°45′35.8″, 104°16′34.8″; [9°44′56.2″, 104°16′28.0″; 9°44′55.1″, 104°16′27.5″]
Segment C	9°38′54.9″, 104°15′32.4″
Segment G	9°16′47.2″, 104°13′08.1″
Grey smoker	
Segment B1:	[9°50′25.0″, 104°17′30.1″; 9°50′24.0″, 104°17′29.9″]; 9°50′17.3″, 104°17′28.8″
Segment B2:	9°47′10.3″, 104°16′57.8″; 9°46′30.9″, 104°16′47.6″; [9°45′35.8″, 104°16′34.8″; 9°45′35.4″, 104°16′35.0″; 9°45′35.0″, 104°16′36.7″; 9°45′34.8″, 104°16′34.9″; 9°45′32.4″, 104°16′34.7″]
White smoker	
Segment B1:	9°50′34.9″, 104°17′31.6″; [9°50′24.6″, 104°17′30.1″; 9°50′22.3″, 104°17′29.5″]; 9°50′17.3″, 104°17′28.8″
Segment B2:	[9°47′33.5″, 104°17′01.2″; 9°47′32.6″, 104°17′00.6″; 9°47′32.5″, 104°17′00.7″; 9°47′31.8″, 104°17′00.4″]; 9°45′35.0″, 104°16′36.7″
Smoke plume	
Segment B1:	9°51′22.2″, 104°17′39.2″; 9°50′15.8″, 104°17′28.4″
Segment B2:	[9°47′32.5″, 104°17′00.9″; 9°47′32.4″, 104°17′00.1″]; 9°47′31.9″, 104°17′00.0″; 9°46′31.5″, 104°16′48.4″; [9°44′56.9″, 104°16′29.0″; 9°44′56.8″, 104°16′27.9″; 9°44′55.7″, 104°16′28.8″; 9°44′54.2″, 104°16′27.4″]; [9°44′50.8″, 104°16′26.6″; 9°44′49.7″, 104°16′27.1″]
Segment C:	9°40′49.2″, 104°15′53.7″
Segment E1:	[9°33′31.6″, 104°14′55.0″; 9°33′31.4″, 104°14′54.9″; 9°33′31.3″, 104°14′55.0″]
Segment E2:	9°30′56.9″, 104°14′38.3″

[a] High temperature inferred from association with sulfide mineral precipitation; see text.
Latitude given in degrees N; longitude in degrees W.
Brackets ([ ]) indicate areas where vent spacing is less than 100 m (one second of latitude ≃ 30 m).

of the axial zone where evidence of past or present vent activity, including occurrences of vent animals, is virtually absent. Considering the survey area as a whole, we report the following observations:

(1) The total number of active high T vents detected in the Venture Hydrothermal Fields is large (= 45; Table 3A). The actual number of vents may be even higher than we report since areal coverage of the axial zone by the ARGO survey is less than 100%. We have grouped these vents into active vent "areas" in which the maximum separation between vents is $\leqslant$ 100 m (Table 3A, B). Along the 44 km of ridge axis surveyed north of 9°30′N, we find 5 black smoker areas, 5 grey smoker areas, 10 additional black or grey smoke plumes, and 5 white smoker areas. Over the 44 km interval, this averages out to one smoker area per 2 km of ridge axis. More than 100 mineral structures (active and inactive chimneys, edifices, and mounds) were found. Though some of these features are quite tall (up to 20 m), none are volumetrically large.

(2) With only one exception, evidence for high T hydrothermal venting is found north of 9°27′N along the shallow (< 2580 m) portion of the ridge where the AMC reflector shoals to < 1.7 km beneath the seafloor (Fig. 3) and is centered beneath the topographic ridge axis [33]. Along the deeper portion of the axis south of 9°27′N, where seismic data show that the magma chamber axis lies west of the topographic ridge axis [17,33], high T venting is almost totally absent (based on ARGO data and Deep Tow camera runs between 9°07′N and 8°55′N [27]). Thus the depth and location of the magma chamber axis may be determining the distribution of high T vents at the 2nd order scale.

(3) With one exception, all high T vents and sulfide deposits are found where the ASC is well-

TABLE 3B

Locations of vents actively discharging low-temperature [a] hydrothermal fluid

Segment A:	9°53′55.1″, 104°17′52.1″; 9°53′36.1″, 104°17′50.4″; 9°53′13.7″, 104°17′50.2″
Segment B1:	9°51′23.7″, 104°17′38.4″; [9°50′57.9″, 104°17′37.1″; 9°50′54.0″, 104°17′39.0″]; [9°50′37.0″, 104°17′32.6″; 9°50′34.9″, 104°17′30.5″; 9°50′34.7″, 104°17′31.3″; 9°50′34.4″, 104°17′30.5″; 9°50′33.7″, 104°17′31.3″; 9°50′33.1″, 104°17′31.4″; 9°50′32.9″, 104°17′32.1″; 9°50′31.6″, 104°17′32.4″; 9°50′30.5″, 104°17′32.1″; 9°50′28.5″, 104°17′30.8″; 9°50′26.5″, 104°17′30.4″; 9°50′25.6″, 104°17′29.1″; 9°50′25.4″, 104°17′30.2″; 9°50′24.8″, 104°17′30.1″; 9°50′24.3″, 104°17′30.0″; 9°50′24.1″, 104°17′28.9″]; [9°50′19.8″, 104°17′28.3″; 9°50′17.7″, 104°17′28.3″]; 9°49′56.7″, 104°17′26.6″; 9°49′30.4″, 104°17′21.8″
Segment B2:	[9°48′25.3″, 104°17′10.9″; 9°48′22.1″, 104°17′09.9″]; 9°47′54.8″, 104°17′06.9″; [9°47′44.9″, 104°17′03.8″; 9°47′44.5″, 104°17′02.7″; 9°47′44.5″, 104°17′03.6″]; [9°47′35.5″, 104°17′01.1″; 9°47′32.9″, 104°17′00.4″; 9°47′32.9″, 104°17′00.9″; 9°47′32.5″, 104°17′00.9″; 9°47′32.4″, 104°17′00.1″; 9°47′32.2″, 104°17′00.6″; 9°47′31.9″, 104°17′00.0″; 9°47′30.4″, 104°17′00.1″; 9°47′27.5″, 104°16′59.9″; 9°47′25.1″, 104°16′59.3″; 9°47′24.2″, 104°17′00.5″; 9°47′23.7″, 104°16′58.3″]; 9°47′09.0″, 104°16′57.5″; [9°46′33.2″, 104°16′48.9″; 9°46′31.5″, 104°16′48.4″]; 9°45′34.8″, 104°16′34.9″; 9°45′22.7″, 104°16′33.0″; 9°45′14.8″, 104°16′31.6″; 9°44′56.5″, 104°16′27.7″; [9°44′51.4″, 104°16′26.0″; 9°44′50.5″, 104°16′25.7″]
Segment C:	9°41′24.2″, 104°16′03.0″; [9°40′52.7″, 104°15′53.6″; 9°40′50.7″, 104°15′54.2″; 9°40′49.2″, 104°15′53.7″]; 9°39′01.7″, 104°15′33.9″; 9°37′33.7″, 104°15′22.7″
Segment E1:	[9°33′31.9″, 104°14′54.9″; 9°33′31.4″, 104°14′54.9″]; [9°33′11.3″, 104°14′55.0″; 9°33′10.9″, 104°14′54.5″; 9°33′10.2″, 104°14′54.5″; 9°33′09.2″, 104°14′54.5″]
Segment E2:	9°32′05.5″, 104°14′48.6″; [9°31′21.8″, 104°14′46.1″; 9°31′20.6″, 104°14′46.0″; 9°31′18.4″, 104°14′45.7″; 9°31′17.6″, 104°14′45.6″; 9°31′17.3″, 104°14′45.9″; 9°31′16.8″, 104°14′45.4″; 9°31′13.5″, 104°14′45.1″]; [9°31′06.9″, 104°14′43.9″; 9°31′06.6″, 104°14′44.7″]; [9°30′29.1″, 104°14′41.1″; 9°30′26.4″, 104°14′39.5″]; [9°30′21.7″, 104°14′36.5″; 9°30′21.6″, 104°14′35.8″; 9°30′20.8″, 104°14′35.8″]; 9°29′43.4″, 104°14′29.7″
Segment G:	9°16′48.0″, 104°13′08.8″; 9°16′34.2″, 104°13′04.8″; 9°16′27.1″, 104°13′05.0″; 9°15′21.1″, 104°13′15.6″
Segment H:	9°11′38.3″, 104°12′49.8″

[a] Diffuse, cloudy effluent; low temperature inferred from absence of visible sulfide mineral precipitation; see text.
Latitude given in degrees N; longitude in degrees W.
Brackets ([ ]) indicate areas where vent spacing is less than 100 m (one second of latitude ≃ 30 m).

developed (Fig. 3), and almost all occur on or near the scarps bounding the ASC. It seems that the enhanced permeability of the crust along the ASC margins may play an important role in the geometry of fluid circulation by channeling the hot fluids at depth to the seafloor.

(4) Consistent with (2) and (3), the greatest density of high-temperature vents is found along Segment B where the ASC is a narrow smoking slot, less than 70 m wide, and where the AMC reflector rises to its shallowest depths.

(5) A reasonably good correlation between young lavas, low fissure density, and hydrothermal vents is observed throughout the survey area. South of 9°28′N, the sole smoker found (at 9°16.8′N) is in the only area of extremely fresh, unfissured lavas. No ASC is present at this site. (A detailed survey here established that the solitary black smoker is confined within an area less than 15 m across. It is not associated with mineral deposits or animals, and may be a very recently developed vent.) All of the hydrothermal gaps occur where the axial lavas are Ages 1.5 or older, and where fissuring of the seafloor is extensive. The only case where this is not true is at 9°17′–21′N, where surface lava flows may have travelled

downslope several kilometers along strike from their source. Along Segment E, lavas also are Ages 1.5–1.7, and fissure density is relatively high. Active venting has not yet ceased along this segment; however, an extensive field of inactive deposits extending south and slightly north of the region of active venting suggests that Segment E activity is waning.

(6) Although roughly 40% of our tracks lie outside the ASC, and though two transects were made out into older off-axis terrain, we saw no evidence for active venting outside the axial zone. It seems that the ASC is strongly controlling high T venting, and that deposits formed along the ASC are buried by lava flows before moving more than 100 m off-axis. Frequent burial of deposits may explain why we find numerous small-tonnage mineral deposits, similar to deposits in vent fields on the fast-spreading EPR at 12–13°N [48], but no large mineral deposits like those found on the medium-rate northern Juan de Fuca Ridge and Galapagos Rift and slow-spreading Mid-Atlantic Ridge [19,45–47].

5.3. *Abundance and distribution of vents: 4th order features*

(1) The boundaries of high T vent areas and hydrothermal gaps in Fig. 1 correspond amazingly well with the segment boundaries defined by bends or small offsets in the ridge axis (Table 2). Our data thus show an along-strike segmentation of hydrothermal circulation which agrees well with morphotectonic/structural segmentation at the 4th order scale.

(2) The number of active vents and the ratio of active vents to inactive deposits varies from segment to segment. From this we infer that the fields on different segments are in different stages of development. The single black smoker at 9°16.8′N has no associated mineral deposits or faunal communities and may represent the initiation of high T activity in an area of very recent volcanism. The numerous high T vents and deposits along Segment B suggest a well-developed hydrothermal field at the height of its activity. The sparse, active high T vents and abundant inactive mineral deposits along Segment E represent a waning hydrothermal system. The estimated ages of associated lavas and extent of fissuring in these areas are consistent with the interpretation that hydrothermal venting onto the seafloor most often develops soon after the end of an eruption and may continue in the area for up to several hundred years if no new eruptions occur. The idea that 4th order segments are in different stages of a volcanic–hydrothermal–tectonic cycle has, in fact, been tested already by dating of sulfide deposits on either side of the Deval on the EPR crest at 12°46′N [53]. North of the Deval at 12°46′N on the EPR, deposits ranging in age from 0–78 years are associated with fresh ponded lavas; south of the Deval, densely fissured older lavas are associated with inactive sulfide deposits ranging in age from 140 to 2000 years.

(3) Above the portion of the ridge where the magma chamber shallows (north of 9°27′N), high T activity occurs discontinuously in discrete areas extending along the margin of the ASC for distances ranging from a few hundred meters to approximately 10 km. These areas are separated from one another along-strike by similar distances. In contrast, vent biota are distributed more continuously, albeit sparsely in places, along ~ 70% of the axial zone (Fig. 1). Since the vent fauna are probably a very sensitive indicator of where there is diffuse, low-level leakage of hydrothermal fluids from the seafloor, their distribution suggests that some diffuse venting is occurring along much of the axial zone. Figure 1 shows hydrothermal gaps where vent animal occurrences are not observed. In fact there are only six small gaps where absolutely no vent animals were seen, none of which extends along strike for more than 3 km. Variations in the abundance of vent biota along the ridge crest, with the largest concentrations occurring near localized areas of high T venting, suggest that the fluid flux from diffuse venting is variable along the axial zone.

5.4. *Discussion of 4th order segmentation of hydrothermal activity and the implications of vent distribution for geometry of circulation*

The close correspondence between the boundaries of morphotectonic/structural 4th order segments and the boundaries of hydrothermal fields and gaps is striking. From this correspondence we infer that hydrothermal circulation is controlled by the same phenomenon that produces 4th order

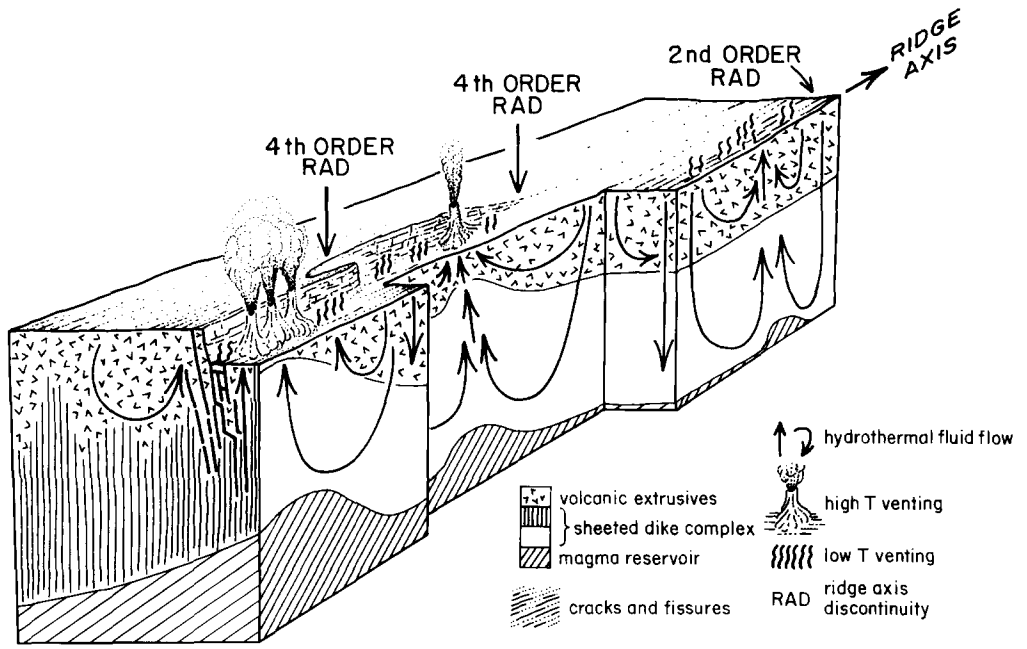

Fig. 7. Schematic sketch of hydrothermal flow geometry proposed for a fast-spreading ridge crest, consistent with vent distribution observed in the Venture Hydrothermal Fields, EPR crest 9°09′–54′N. Cross-section parallel to the ridge axis follows one side of the ASC until it disappears, then shifts to the ridge axis and follows a highly fissured segment of the axial zone. This diagram represents an integrated model of ridge crest magmatic/tectonic activity and hydrothermal flow that includes the following features: (1) shallow 3-D circulation in the more permeable volcanics, superimposed on top of (2) 2-D ridge-parallel circulation in the relatively impermeable sheeted dike complex along cracked zones of enhanced permeability (e.g., along ASC margins and along deep axial fissures); (3) along-axis segmentation of deep hydrothermal flow, due to (a) the spacing of recent magmatic intrusions (represented as bumps on the magma reservoir and on the upper bound of dike complex) and (b) lateral spatial shifts along-strike in zones of enhanced permeability in the dikes; (4) greater abundance of high T vents above shallower segments of the axial magma reservoir. This model emphasizes that the interaction between thermal and permeability fields governs hydrothermal flow at MOR crests.

ridge segmentation, most likely, the locations of the most recent dike swarms feeding eruptions along the axial zone. It is likely that the upward bending of isotherms above zones of recent shallow dike intrusion thermally drives fluids in the dike complex toward the seafloor. On this basis we propose that 4th order segmentation of hydrothermal venting is governed by the thermal perturbations imposed by small-scale, shallow magmatic intrusion (i.e. diking; Fig. 7), just as vent distribution at the 2nd order scale appears to be governed by the regional thermal regime corresponding to the location and depth of the axial magma chamber. Seismic data from the survey area confirm that narrow high-velocity zones, presumed to be dikes, lie only 300–500 m directly beneath the ridge axis ([17,54]; M. Purdy, pers. commun.).

Whether the fluids circulating to depth in the dike section convect predominantly parallel or perpendicular to the ridge axis is an important question. The margins of the ASC provide zones of relatively higher permeability along which vigorous ridge-parallel circulation in the sheeted dikes could occur, and the observed gaps between high T vent areas along the ASC may be cooler and/or more permeable areas in which recharge occurs along the axis. However, the rather continuous diffuse discharge of fluids along the axial zone, inferred from the distribution of vent animals, must be recharged either in the very localized gaps along the axis (a possibility which is hydrodynamically unlikely and for which there is no independent evidence to date), or somewhere off-axis by ridge-perpendicular flow. These observations may be reconciled by invoking a two-

layer model of circulation (Fig. 7) similar to that previously proposed for fossil hydrothermal systems in the Oman ophiolite, in which three-dimensional shallow circulation of low T fluids in the volcanics is superimposed on top of deeper, ridge-parallel circulation of high T fluids down into the sheeted dikes ([55–57]; and Haymon et al., in prep.).

6. Conclusions

We have established the distribution of hydrothermal features and the volcanic/tectonic characteristics of the EPR axial zone along an 83 km length of a fast-spreading 2nd order ridge segment. We conclude that the distribution of hydrothermal activity at the 2nd order scale is largely controlled by: (1) the depth and location of the magma chamber axis relative to the topographic ridge axis, and (2) the development of an axial summit caldera. 4th order segmentation of the ridge crest is clearly observed in the fine-scale characteristics of the axial zone as well as in the behavior of the ridge axis. The morphotectonic/structural segmentation of the ridge crest at the 4th order scale matches remarkably well with along-strike variability observed in axial hydrothermal activity. We attribute both morphotectonic/structural 4th order segmentation and hydrothermal 4th order segmentation to the spatial distribution of recent dike intrusions along the ridge crest. The 4th order segments appear to be in various stages of magmatic, tectonic, and hydrothermal development, and we postulate the existence of a typical volcanic–hydrothermal–tectonic cycle on fast-spreading ridge crests that begins with diking and eruption, followed by magmatic drainback or drainage and gravitational collapse, possible development of an ASC, and the onset of hydrothermal activity. The hydrothermal activity may wax and continue for up to several hundred years where an ASC is present. The latest phase in the cycle is extensive tectonic fissuring, widening of the ASC (if present) by mass wasting along the margins, and waning of hydrothermal venting, due to cooling of the heat source and increased dilution of hydrothermal fluids with cold seawater penetrating into the fissured crust. When the time interval between eruptions is significantly less than 1000 years, the late tectonic phase may not develop.

Acknowledgements

This research would not have been possible without the dedicated efforts of the ARGO technical group at the WHOI Deep Submergence Laboratory including: A. Bowen, T. Crook, S. Gegg, D. Gleason, W. Lange, K. Stewart, and the at-sea ARGO data acquisition group. We also thank Captain Tom Desjardins and the crew and staff of SIO's R/V *Thomas Washington* for their excellent support. Special acknowledgements go to Tom O'Brien (USGS) for assistance with sonar data acquisition and processing; Ralph Hitz, Nell Beedle, and Steve Miller for help with data management and processing; and to Ginger Barth, Dan Scheirer, Charlie Weiland, Gene Pillard, and Tom Ivey for courageous watchstanding and general help at sea. We also thank John Bender, Dale Chayes, Dave Gallo, Bob Ballard, Kim Kastens, Charlie Langmuir, and Bill Ryan for pre-cruise logistical assistance; Angela Macias and Antoinette Padgett for their expert drafting and word processing; and, Dave Crouch for his excellent illustrations. The manuscript benefitted from the comments of two anonymous reviewers. This research was an Ocean Drilling Program site survey supported by The National Science Foundation, grants OCE-88–17587 (R.M.H.) and OCE-88–17658 (D.J.F.).

LDGO Contribution No. 4763.

References

1 D.L. Williams, R.P. von Herzen, J. Sclater and R.N. Anderson, Galapagos spreading center; Lithospheric cooling and hydrothermal circulation, Geophys. J.R. Astron. Soc. 38, 587–608, 1974.

2 T.J. Wolery and N.H. Sleep, Hydrothermal circulation and geothermal flux at mid-ocean ridges, J. Geophys. Res. 84, 249–275, 1976.

3 J.M. Edmond, C. Measures, R.E. McDuff, L.H. Chan, R. Collier, R. Grant, B. Gordon, L.I. and J.B. Corliss, Ridge crest hydrothermal activity and the balances of the major and minor elements in the ocean; the Galapagos data, Earth Planet. Sci. Lett. 46, 1–18, 1979.

4 K.L. Von Damm, J.M. Edmond, B. Grant, C.I. Measures and R.F. Weiss, Chemistry of submarine hydrothermal solutions at 21°N, East Pacific Rise, Geochim. Cosmochim. Acta 49, 2197–2220, 1985.

5 M.A. Tivey and H.P. Johnson, High-resolution geophysical studies of oceanic hydrothermal systems, Rev. Aquatic Sci. 1, 473–496, 1989.
6 R. Haymon, Hydrothermal processes and products on the Galapagos Rift and East Pacific Rise, in: The Geology of North America, Vol. N, E.L. Winterer, D.M. Hussong and R.W. Decker, eds., pp. 125–143, Geological Society of America, Boulder, Colo., 1989.
7 R.A. Koski, D.A. Clague and E. Oudin, Mineralogy and chemistry of massive sulfide deposits from the Juan de Fuca Ridge, Geol. Soc. Am. Bull. 95, 930–945, 1984.
8 R.R. Hessler and J.W.M. Smithey, The distribution and community structure of megafauna at the Galapagos Rift hydrothermal vents, in: Hydrothermal Processes at Seafloor Spreading Centers, P.A. Rona, K. Bostrom, L. Laubier and K.L. Smith, eds., pp. 735–770, Plenum Press, New York, N.Y., 1983.
9 F.N. Speiss, K.C. Atwater, R. Ballard, A. Carranza, D. Cordoba, C. Cox, V. Diaz-Garcia, J. Francheteau, J. Guerrero, J. Hawkins, R. Haymon, R. Hessler, T. Juteau, M. Kastner, R. Larson, B. Luyendyk, J. Macdougall, S. Miller, W. Normark, J. Orcutt and C. Rangin, East Pacific Rise: hot springs and geophysical experiments, Science 207, 1421–1433, 1980.
10 J. Corliss, J. Dymond, L.I. Gordon, J. Edmond, R.P. von Herzen, P. Richard, R.D. Ballard, K. Green, D. Williams, A. Bainbridge, K. Crane and T.H. van Andel, Submarine thermal springs on the Galapagos rift, Science 203, 1073–1082, 1979.
11 K.C. Macdonald, J.-C. Sempere and P.J. Fox, East Pacific Rise from Siqueiros to Orozco fracture zones: along-strike continuity of axial neovolcanic zone and structure and evolution of overlapping spreading centers, J. Geophys. Res. 89, 6049–6069, 1984.
12 C.M. Langmuir, J.F. Bender and R. Batiza, Petrological and tectonic segmentation of the East Pacific Rise, 5°30′–14°30′N, Nature 322, 422–429, 1986.
13 R.S. Detrick, P. Buhl, E. Vera, J. Orcutt, J. Madsen and T. Brocher, Multi-channel seismic imaging of a crustal magma chamber along the East Pacific Rise, Nature 326, 35–41, 1987.
14 K.C. Macdonald, P.J. Fox, L.J. Perram, M.F. Eisen, R.M. Haymon, S.P. Miller, S.M. Carbotte, M.-H. Cormier and A.N. Shor, A new view of the mid-ocean ridge from the behaviour of ridge-axis discontinuities, Nature 335, 217–225, 1988.
15 P. Lonsdale, Linear volcanos along the Pacific–Cocos plate boundary, 9°N to the Galapagos triple junction, Tectonophysics 116, 255–279, 1985.
16 J.A., Whitehead, H.J.B.Dick and H. Schouten, A mechanism for magmatic accretion under spreading centers, Nature 312, 146–148, 1984.
17 D.R. Toomey, G.M. Purdy, S.C. Solomon and W.S.D. Wilcock, The three-dimensional seismic velocity structure of the East Pacific Rise near latitude 9°30′N, Nature 347, 639–645, 1990.
18 R.D. Ballard, E. Uchupi, D.K. Blackman, J.L. Cheminee, J. Francheteau, R. Hekinian, W.C. Schwab and H. Sigurdsson, Geological mapping of the East Pacific rise axis (10°19′–11°53′N) using the ARGO and ANGUS imaging systems, Can. Mineral. 26, 467–486, 1988.
19 R.W. Embley, I.R. Jonasson, M.R. Perfit, J.M. Franklin, M.A. Tivey, A. Malahoff, M.F. Smith and T.J.G. Francis, Submersible investigation of an extinct hydrothermal system on the Galapagos Ridge: sulfide mounds, stockwork zone, and differentiated lavas, Can. Mineral. 26, 517–539, 1988.
20 R. Hekinian, V. Renard and J.L. Cheminee, Hydrothermal deposits on the East Pacific Rise near 13°N: geological setting and distribution of active sulfide chimneys, in: Hydrothermal Processes at Spreading Centers, P.A. Rona, K. Bostrom, L. Laubier and K.L. Amith, eds., pp. 571–594, Plenum Press, New York, N.Y., 1984.
21 S.E. Harris and R.D. Ballard, ARGO: capabilities for deep ocean exploration, 6–8 pp., IEEE, Washington, D.C., 1986.
22 S.E. Harris, R.H. Squires and E.M. Bergeron, Underwater imagery using an electronic still camera, 1242–1245 pp., IEEE, Washington, D.C., 1987.
23 T.F. McConachy, R.D. Ballard, M.J. Mottl and R.P. von Herzen, Geologic form and setting of a hydrothermal vent field at lat 10°56′N, East Pacific Rise: a detailed study using ANGUS and ALVIN, Geology 14, 295–298, 1986.
24 K.D. Klitgord and J. Mammerickx, Northern East Pacific Rise: magnetic anomaly and bathymetric framework, J. Geophys. Res. 87, 6725–6750, 1982.
25 P. Lonsdale, Overlapping rift zones at the 5.5°S offset of the East Pacific Rise, J. Geophys. Res. 88, 9393–9406, 1983.
26 K.C. Macdonald, R.M. Haymon, S.P. Miller, J.-C. Sempere and P.J. Fox, Deep-Tow and Sea Beam studies of dueling propagating ridges on the East Pacific Rise near 20°40′S, J. Geophys. Res. 93, 2875–2898, 1988.
27 J.C. Sempere and K.C. Macdonald, Deep-tow studies of the overlapping spreading centers at 9°03′N on the East Pacific Rise, Tectonics, 5, 881–900, 1986.
28 K.C. Macdonald and P.J. Fox, The axial summit graben and cross-sectional shape of the East Pacific Rise as indicators of axial magma chambers and recent volcanic eruptions, Earth Planet. Sci. Lett. 88, 119–131, 1988.
29 K.C. Macdonald, P.J. Fox, S. Carbotte, M. Eisen, S. Miller, L. Perram, D. Scheirer, S. Tighe and C. Weiland, The East Pacific Rise and its flanks 8°–17°N: history of segmentation, propagation and spreading direction based on SeaMarc II and Sea Beam studies, Mar. Geophys. Res., in press.
30 D.J. Fornari, M.R. Perfit, J.F. Allan, R. Batiza, R. Haymon, A. Barone, W.B.F. Ryan, T. Smith, T. Simkin and M.A. Luckman, Geochemical and structural studies of the Lamont seamounts: seamounts as indicators of mantle processes, Earth Planet. Sci. Lett. 89, 63–83, 1988.
31 J. Brodholt and R. Batiza, Magma supply processes in the tomography area (9°30′N) of the EPR, EOS Trans. Am. Geophys. Union 69, 1475, 1988.
32 K.A. Kastens, W.B.F. Ryan and P.J. Fox, Structural and volcanic expression of a fast slipping ridge-transform boundary: Sea MARC I and photographic surveys at the Clipperton transform fault, J. Geophys. Res. 1986, 3469–3488, 1986.
33 J.C. Mutter, G.A. Barth, P. Buhl, R.S. Detrick, J. Orcutt and A. Harding, Magma distributions across ridge axis discontinuities on the East Pacific Rise from seismic images, Nature 336, 156–158, 1988.
34 D.J. Fornari, W.B.F. Ryan and P.J. Fox, The evolution of

craters and calderas on young seamounts: insights from SeaMARC I and Sea Beam sonar surveys of a small seamount group near the axis of the East Pacific Rise at ~10°N, J. Geophys. Res. 89, 11069–11083, 1984.

35 R.D. Ballard, J. Francheteau, T. Juteau, C. Rangin and W. Normark, East Pacific Rise at 21°N; the volcanic, tectonic, and hydrothermal processes of the central axis, Earth Planet. Sci. Lett. 55, 1–10, 1981.

36 P. Lonsdale and F.N. Spiess, Deep-tow observations at the East Pacific Rise, 8°45′N, and some interpretations, in: B.R. Rosendahl, R. Hekinian et al., Initial Reports of the Deep Sea Drilling Project, 54, pp. 43–62, U.S. Government Printing Office, Washington, D.C., 1980.

37 R.D. Ballard and J. Francheteau, The relationship between active sulfide deposition and the axial processes of the mid-ocean ridge, Mar. Technol. Soc. J. 16, 8–20, 1982.

38 P. Gente, J.M. Auzende, V. Renard, Y. Fouquet and D. Bideau, Detailed geological mapping by submersible of the East Pacific Rise axial graben near 13°N, Earth. Planet. Sci. Lett. 78, 224–236, 1986.

39 J.A. Karson, G. Thompson, S.E. Humphris, J.M. Edmond, W.B. Bryan, J.R. Brown, A.T. Winters, R.A. Pockalny, J.F. Casey, A.C. Campbell, G. Klinkhammer, M.R. Palmer, R.J. Kinzler and M.M. Sulanowska, Along-axis variations in seafloor spreading in the Mark area, Nature, 328, 681–685, 1987.

40 D.S. Stakes, J.W. Shervais and C.A. Hopson, The volcanic–tectonic cycle of the Famous and Amar valleys, Mid-Atlantic Ridge (36°47′N): evidence from basalt glass and phenocryst compositional variations for a steady state magma chamber beneath the valley midsections, AMAR 3, J. Geophys. Res. 89, 6995–7028, 1984.

41 P. Lonsdale, Structural geomorphology of a fast-spreading rise crest: the East Pacific Rise near 3°25′S, Mar. Geophys. Res. 3, 251–293, 1977.

42 M.P. Ryan, R.Y. Koyanagi and R.S. Fiske, Modeling the three-dimensional structure of macroscopic magma transport systems: applications to Kilauea, Hawaii, J. Geophys. Res. 86, 71111–7129, 1981.

43 K. Crane, F. Aikman III and J.-P. Foucher, The distribution of geothermal fields along the East Pacific Rise from 13°10′N to 8°20′N: implications for deep seated origins, Mar. Geophys. Res. 9, 211–236, 1988.

44 A.C. Campbell, M.R. Palmer, G.P. Klinkhammer, T.S. Bowers, J.M. Edmond, J.R. Lawrence, J.F. Casey, G. Thompson, S. Humphris, P. Rona and J. Karson, Chemistry of hot springs on the Mid-Atlantic Ridge, Nature 335, 514–519, 1988.

45 M.K. Tivey and J.R. Delaney, Growth of large sulfide structures on the Endeavor Segment of the Juan de Fuca Ridge, Earth Planet. Sci. Lett. 77, 303–317, 1986.

46 P.A. Rona, G. Klinkhammer, T.A. Nelsen, J.H. Trefry and H. Elderfield, Black smokers, massive sulphides and vent biota at the Mid-Atlantic Ridge, Nature 321, 33–37, 1986.

47 G. Thompson, W.B. Bryan, R. Ballard, K. Hamuro and W.G. Melson, Morphology, mineralogy and chemistry of hydrothermal deposits from the TAG area, 26°N Mid-Atlantic Ridge, Chem. Geol. 49, 243–257, 1985.

48 R. Hekinian and Y. Fouquet, Volcanism and metallogenesis of axial and off-axial structures on the East Pacific Rise near 13°N, Econ. Geol. 80, 221–249, 1985.

49 A.C. Campbell, T.S. Bowers, C.I. Measures, K.K. Falkner, M. Khadem and J.M. Edmond, A time series of vent fluid compositions from 21°N, East Pacific Rise (1979, 1981, 1985), and the Guaymas Basin, Gulf of California (1982, 1985), J. Geophys. Res. 93, 4537–4549, 1988.

50 G. Michard, F. Albarede, A. Michard, J.F. Minster, J.L. Charlou and N. Tan, Chemistry of solutions from the 13°N East Pacific Rise hydrothermal site, Earth Planet. 67, 297–307, 1984.

51 T.S. Bowers, A.C. Campbell, C.I. Measures, A.J. Spivack, M. Khadem and J.M. Edmond, Chemical controls on the composition of vent fluids at 13°–11°N and 21°N, East Pacific Rise, J. Geophys. Res. 93, 4522–4536, 1988.

52 K.L. Von Damm, Systematics of and postulated controls on submarine hydrothermal solution chemistry, J. Geophys. Res. 93, 4551–4561, 1988.

53 C. Lalou, E. Brichet and R. Hekinian, Age dating of sulfide deposits from axial and off-axial structures on the East Pacific Rise near 12°50′N, Earth Planet. Sci. Lett. 75, 59–71, 1985.

54 E.E. Vera, J.C. Mutter, P. Buhl, J.A. Orcutt, A.J. Harding, M.E. Kappus, R.S. Detrick and T.M. Brocher, The structure of 0- to 0.2-m.y.-old oceanic crust at 9°N on the East Pacific Rise from expanded spread profiles, J. Geophys. Res. 95, 15529–15556, 1990.

55 P. Nehlig and T. Juteau, Flow porosities, permeabilities and preliminary data on fluid inclusions and fossil thermal gradients in the crustal sequence of the Sumail ophiolite (Oman), in: The Ophiolites of Oman, F. Boudier and A. Nicolas, eds., Tectonophysics 151, 199–221, 1988.

56 R.M. Haymon and R.A. Koski, A 3-D model of along-axis hydrothermal circulation, discharge, and mineralization in the Bayda hydrothermal system, N. Oman ophiolite, EOS Trans. Am. Geophys. Union 68, 1545, 1987.

58 S.A. Tighe, R.S. Detrick, P.J. Fox, C.H. Langmuir, J.C. Mutter, W.B. Ryan and R.C. Tyce, East Pacific Rise Data Synthesis Final Report, Vol. 1, Joint Oceanographic Institutions, Inc., Washington, D.C., 1988.

59 G.M. McMurtry, J.J. Veeh and C. Moser, Sediment accumulation rate and patterns on the northwest Nazca plate, in: Nazca Plate: Crustal Formation and Andean Convergence, L.D. Kulm, J. Dymond, E.J. Dasch, D.M. Husssong, eds., Mem. Geol. Sci. Am. 154, 211–250, 1981.